Distortion product emissions from a cochlear model with nonlinear mechanoelectrical transduction in outer hair cells

Yi-Wen Liu and Stephen T. Neely
Boys Town National Research Hospital, 555 North 30th Street, Omaha, Nebraska 68131

(Received 10 November 2009; revised 4 February 2010; accepted 5 February 2010)

A model of cochlear mechanics is described in which force-producing outer hair cells (OHC) are embedded in a passive cochlear partition. The OHC mechanoelectrical transduction current is nonlinearly modulated by reticular-lamina (RL) motion, and the resulting change in OHC membrane voltage produces contraction between the RL and the basilar membrane (BM). Model parameters were chosen to produce a tonotopic map typical of a human cochlea. Time-domain simulations showed compressive BM displacement responses typical of mammalian cochleae. Distortion product (DP) otoacoustic emissions at $2f_1-f_2$ are plotted as isolevel contours against primary levels (L_1,L_2) for various primary frequencies f_1 and f_2 $(f_1<f_2)$. The L_1 at which the DP reaches its maximum level increases as L_2 increases, and the slope of the "optimal" linear path decreases as f_2/f_1 increases. When primary levels and f_2 are fixed, DP level is band passed against f_1. In the presence of a suppressor, DP level generally decreases as suppressor level increases and as suppressor frequency gets closer to f_2; however, there are exceptions. These results, being similar to data from human ears, suggest that the model could be used for testing hypotheses regarding DP generation and propagation in human cochleae.
 [DOI: 10.1121/1.3337233]

PACS number(s): 43.64.Kc, 43.64.Ld, 43.64.Jb [BLM] Pages: 2420–2432

I. INTRODUCTION

Nonlinear growth is characteristic of healthy mammalian cochleae (Rhode, 1971). Introducing nonlinearity to the damping coefficient of cochlear models (Kim *et al.*, 1973; Hall, 1974) enabled the simulation of distortion products (DPs) and other nonlinear responses. In several subsequent studies, the damping coefficient was allowed to be negative at low intensity so sounds were amplified in a frequency- and place-specific manner. As a result, model responses achieved high sensitivity and sharp tuning typical of mammalian hearing (Davis, 1983; Neely and Kim, 1983, 1986). Since then, understanding of the biophysical foundations for the putative "cochlear amplifier" has improved (see Dallos, 2008, for a review). Models proposed in recent years (Lu *et al.*, 2006; Ramamoorthy *et al.*, 2007; Liu and Neely, 2009; Rabbitt *et al.*, 2009) indicated that outer hair cells (OHCs) likely provide cycle-by-cycle amplification to cochlear traveling waves because of their capabilities to convert mechanical and electrical energy in both directions (Brownell *et al.*, 1985; Hudspeth, 1997). However, these newer results were obtained by linear analysis in the frequency domain; time-domain simulation of DP and other nonlinear responses from these models has not yet been reported.

The goals of the present study are (1) to construct a nonlinear cochlear model that incorporates recent findings in OHC biophysics and (2) to test the model's time-domain response to single and multitone stimuli for a broad range of stimulus conditions. Of particular interest is the simulation of distortion-product otoacoustic emissions (DPOAEs). First observed in late 1970s (Kemp, 1978; Kim *et al.*, 1980), DPOAEs have been measured for a wide range of stimulus frequencies and levels (e.g., Gaskill and Brown, 1990). Damage to the OHCs causes reduction of DPOAEs (Zurek *et al.*, 1982), confirming OHCs' contribution to cochlear nonlinearity. Computer simulation of DPOAE emerged in the 1990s. Using a variation of the Neely and Kim (1986) model, Kanis and de Boer (1993) calculated DP levels via a frequency-domain iterative quasilinear approach. Results suggested that the source of DP is distributed, and that DP travels backward to the middle ear via a slow transverse wave. A later revision of the Neely and Kim (1986) model included an explicit representation of the membrane potential in OHCs (Neely, 1993). Subsequently, simulation of DP was carried out using a time-domain approach (Neely and Stover, 1994); when the frequency of one primary tone (f_2) was fixed while the other $(f_1,f_1<f_2)$ was swept, DP level had a band-pass filtering characteristic similar to that observed in humans and rodents (Brown *et al.*, 1992). When the levels of the primaries were swept, the revised model also produced DPOAE input-output (I/O) functions typical of humans (Neely *et al.*, 2000). In the interim, theoretic treatment of DPOAE was conducted by Talmadge *et al.* (1998) using a frequency-domain, perturbative approach to explain fine structures and the band-pass filtering effect.

The present study is an extension to modeling efforts previously described in a few ways. First, the present model describes OHC biophysics in more detail (Liu and Neely, 2009), which makes it possible to place the nonlinearity specifically in the mechanoelectrical transduction (MET) channel of OHCs. The advantage of modeling OHCs biophysics is discussed in Sec. V. Second, DPOAEs for a wide range of primary levels and primary frequencies were simulated so

 0001-4966/2010/127(4)/2420/13/$25.00

TABLE I. Parameters for cochlear mechanics.

	Meaning (unit)	Base	Mid	Apex
	Organ of Corti mechanical parameters			
M	Mass in OHC load impedance (g)	2.8×10^{-8}	5.0×10^{-7}	2.8×10^{-5}
R	Resistance in OHC load impedance (g s^{-1})	9.4×10^{-4}	9.2×10^{-4}	2.7×10^{-3}
K	Stiffness in OHC load impedance (g s^{-2})	200	11	0.76
m	BM mass per unit area (g cm^{-2})	3.8×10^{-5}	2.8×10^{-4}	2.1×10^{-3}
r	BM resistance per unit area (g s^{-1} cm^{-2})	1.5	3.2	8.6
k	BM stiffness per unit area (g s^{-2} cm^{-2})	5.9×10^{5}	4.0×10^{4}	1.6×10^{3}
	Outer hair cell electromechanical properties			
α_d	MET's sensitivity to RL displacement (A/m)	1.6×10^{-3}	6.2×10^{-4}	2.0×10^{-4}
α_v	MET's sensitivity to RL velocity (C/m)	4.4×10^{-6}	1.8×10^{-6}	6.8×10^{-7}
$I_{\max}$	Maximum range of OHC receptor current (pA)	670	320	83
T	Piezoelectric transformer ratio (m/C)	2.4×10^{6}	2.4×10^{6}	2.4×10^{6}
G	Membrane conductance (nS)	91	51	33
C	Membrane capacitance (pF)	14	32	79
C_g	Gating capacitance (pF)	18	33	70
	Physical dimensions			
A	Cochlear cross-sectional area (cm^2)	6.3×10^{-2}	1.4×10^{-2}	3.1×10^{-3}
w	BM width (cm)	0.031	0.040	0.051
L	Length of cochlea (cm)	3.5		

results can be compared to data recently reported by Johnson *et al.* (2006). In addition, model responses to three-tone stimuli in a DP suppression paradigm are compared to data from normal-hearing humans (Rodríguez *et al.*, 2010).

It is noteworthy that, although DPOAE is a robust phenomenon routinely used for clinical purposes, there is still a debate regarding DP propagation. The existence of slow-traveling waves has been challenged (Nobili *et al.*, 2003), and transmission-line modeling efforts (e.g., Neely and Kim, 1983) have been criticized. Nobili *et al.* (2003) proposed that the motion of the stapes is coupled to the basilar membrane (BM) via fluid compressional waves. This theory found supports from a laser-scanning measurement of BM motion (Ren, 2004), which seems to suggest reverse propagation of DPs via compressional (fast) waves. However, the interpretation was based on the phase velocity of DP and its flaws have been noted (Shera *et al.*, 2007). By simultaneous measurements of DPOAE and intracochlear acoustic pressure, Dong and Olson (2008) found evidence for reverse-traveling waves in the phase response of DPOAE relative to the phase response of intracochlear DPs. As will be described in Sec. II, the macromechanical model for the present study is a transmission-line model. Therefore, results presented in this paper are based on the slow-traveling wave theory.

Besides DPs, a plethora of nonlinear phenomena has been observed in cochlear mechanics. Some of them have been reproduced in computational models, including level-dependent latency of transient responses (Neely, 1988), instantaneous-frequency glide in transient responses (Hubbard *et al.*, 2003), asymmetric onset and offset response time (Zhang *et al.*, 2009), and an in-depth investigation (Ku *et al.*, 2009) of spontaneous otoacoustic emissions (SOAEs). Transient responses are beyond the scope of this paper, while generation of SOAEs will be discussed in Sec. V.

The rest of this paper is organized as follows. Models for OHC biophysics, cochlear mechanics, and middle-ear mechanics are described in Sec. II. Parameter selection and methods for time-domain simulation are described in Sec. III. Model responses to single and multitone stimuli are reported in Sec. IV. Discussion is given in Sec. V, followed by conclusions in Sec. VI.

II. MODELS

Sections II A–II C describe the present model for cochlear mechanics, and Sec. II D describes a simple model for the mechanics of the middle ear. Cochlear and middle-ear parameters are listed in Table I and II, respectively.

A. Outer hair cells: Mechanoelectrical transduction

The receptor current that flows into an OHC is modulated by deflection of its hair bundle (HB). We previously proposed to model this as follows (Liu and Neely, 2009):

$$i_r = \alpha_v \dot{\xi}_r + \alpha_d \xi_r, \tag{1}$$

where i_r denotes the receptor current, and ξ_r and $\dot{\xi}_r$ denote the reticular-lamina (RL) displacement and velocity, respectively; tectorial-membrane motion is not considered explicitly in favor for simplicity here.[1] In the present study, Eq. (1) is generalized by introducing nonlinearity to it:

$$i_r = I(\alpha_v \dot{\xi}_r + \alpha_d \xi_r), \tag{2}$$

where $I(\cdot)$ denotes an arbitrary nonlinear function. For the present study, we defined $I(\cdot)$ as an antisymmetric function:

TABLE II. Parameters for middle-ear mechanics.

	Meaning (unit)	Value
	Maleus-incus-eardrum parameters	
A_m	Area of eardrum (cm^2)	0.5
M_m	Effective mass (g)	8.5×10^{-3}
R_m	Effective resistance (g s^{-1})	20
K_m	Effective stiffness (g s^{-2})	1.5×10^{5}
g_m	Maleus-incus lever ratio	0.7
	Incudo-stapedial joint	
R_i	Resistance (g s^{-1})	400
K_i	Stiffness (g s^{-2})	5.0×10^{6}
	Stapes parameters	
A_s	Area of stapes footplate (cm^2)	0.0625
M_s	Effective mass (g)	5.0×10^{-3}
R_s	Effective resistance (g s^{-1})	80
K_s	Effective stiffness (g s^{-2})	5.0×10^{5}
	Round-window parameters	
A_r	Area of round window (cm^2)	0.0625
M_r	Effective mass (g)	5.0×10^{-3}
R_r	Effective resistance (g s^{-1})	20
K_r	Effective stiffness (g s^{-2})	1.5×10^{5}

$$I(\eta) \triangleq I_{\max}\left(\frac{1}{1+\exp(-4\eta/I_{\max})}-\frac{1}{2}\right)=\frac{I_{\max}}{2}\tanh\frac{2\eta}{I_{\max}}, \tag{3}$$

where $\eta=\alpha_v\dot{\xi}_r+\alpha_d\xi_r$. Note that the full range of current output is $I_{\max}$, and the slope of $I(\cdot)$ is unity at the origin:

$$\left.\frac{\partial I}{\partial \eta}\right|_{\eta=0}=1.$$

Experiments have shown that the nonlinear function $I(\cdot)$ should be an asymmetric function because of rectification; i_r is larger when the HB is deflected toward the tallest row of stereocilia than i_r is negative when the HB is rarified (e.g., Corey and Hudspeth, 1983; Ricci *et al.*, 2005). Nevertheless, the nonlinearity given by Eq. (3) was suitable for this study because the main concern was to simulate DP at $2f_1-f_2$, which is an odd-order distortion.[2]

B. Outer hair cells: Electromotility

The present study adopts a one-dimensional (1D) piezoelectric OHC model that we previously proposed (Liu and Neely, 2009). The underlying assumptions of the model are summarized below. First, the receptor current i_r is the sum of capacitive, conductive, and gating components:

$$i_r=C\frac{dV}{dt}+GV+\frac{dQ}{dt}, \tag{4}$$

where C and G are the capacitance and the conductance of the plasmic membrane, respectively, V is the transmembrane potential, and Q is the charge accumulation that accompanies electromotility. Second, the OHC contraction displacement ξ_o is linearly proportional to Q,

$$\xi_o=TQ, \tag{5}$$

where T represents a piezoelectric constant. Finally, Q is a Boltzmann function of $\tilde{V}\triangleq V-Tf_{\mathrm{OHC}}$, where f_{OHC} is a contraction force generated by the OHC.

For the present study, the Boltzmann function $Q(\tilde{V})$ is linearized so the only source of nonlinearity is from the MET channel. Linearization of $Q(\tilde{V})$ is legitimate if $\tilde{V}$ is small in comparison to the voltage scale in the Boltzmann function—this appears to be the case at the stimulus levels of interest (SPL$\leq$100 dB, see Sec. V for further details). Therefore, Eq. (4) can be rewritten as

$$i_r=C\frac{dV}{dt}+GV+C_g\frac{d\tilde{V}}{dt}, \tag{6}$$

where $C_g\triangleq\partial Q/\partial\tilde{V}$ denotes a gating capacitance that is approximately constant in time.

In the present study, it is assumed that the OHC contracts and stretches against a simple mechanical load:[3]

$$f_{\mathrm{OHC}}=M\ddot{\xi}_o+R\dot{\xi}_o+K\xi_o, \tag{7}$$

where M, R, and K are the effective mass, resistance, and stiffness, respectively.

C. Cochlear macromechanics

The macromechanics of the cochlea are governed by Newton's laws and the principle of continuity. In a one-dimensional nonviscous model (Dallos, 1973), Newton's second law requires that

$$\partial_x P=-\frac{\rho}{A}\dot{U}, \tag{8}$$

where P denotes the pressure difference between two cochlear chambers (*scala vestibuli* and *scala tympani*), x denotes the longitudinal direction from base to apex, ρ denotes the effective fluid mass density, A denotes the cross-sectional area of the fluid chamber, and U denotes the volume velocity along the x-direction. The present study assumes that the fluid is incompressible, and the principle of continuity is represented by the following equation[4] (Neely and Liu, 2009):

$$\partial_x U=w\dot{\xi}_r, \tag{9}$$

where w is the width of cochlear partition. The displacement ξ_b of the BM, equal to the sum of ξ_r and ξ_o, is driven by the pressure P:

$$m\ddot{\xi}_b+r\dot{\xi}_b+k\xi_b=-P, \tag{10}$$

where m, r, and k are mass, resistance, and stiffness of BM per unit area.

The boundary condition at the apical end of the cochlea is

$$\partial_x P|_{x=L}=\frac{-\rho}{Am_h}P, \tag{11}$$

where $m_h=110$ g/cm^4 is an acoustic inductance which represents the mass of the fluid at the helicotrema [Puria and

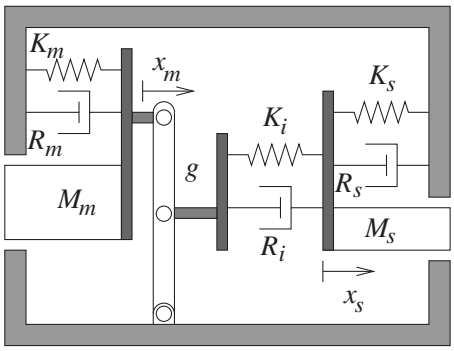

FIG. 1. Schematic diagram of middle-ear mechanics. Pressure and displacement are coupled between the ear canal (to the left) and the cochlear fluid (to the right). Subscript m denotes the malleus-incus-eardrum system, i denotes incudo-stapedial joint, and s denotes stapes.

Allen, 1991, Eq (11)]. The boundary condition at the basal end of the cochlea is

$$\partial_x P|_{x=0} = -\rho \dot{v}_s, \tag{12}$$

where v_s denotes the velocity of the stapes.

D. Modeling the middle ear

The present middle-ear model, adapted from Matthews (1983), is aimed to reproduce adequately the pressure magnitude transfer functions measured from human cadavers (e.g., Puria, 2003; Nakajima *et al.*, 2009) without pursuing other details in middle-ear mechanics. A schematic diagram of the middle ear is shown in Fig. 1. The malleus, the incus, and the eardrum are lumped into one system as suggested by Zwislocki (1962), while any motion on the eardrum that is not coupled to the ossicular chain is ignored. The malleus-incus-eardrum system is characterized by parameters $\{M_m, R_m, K_m\}$. The malleus-incus lever ratio is denoted as g ($g \leq 1$). The incudo-stapedial joint (ISJ) is characterized by parameters $\{R_i, K_i\}$. The stapes and its surrounding structures are represented by parameters $\{M_s, R_s, K_s\}$.

Given the diagram in Fig. 1, the *acoustic pressure*[5] P_{ED} at the eardrum and the cochlear fluid pressure P_{FL} at the stapes are coupled to each other via the following equations:

$$M_m \dot{v}_m = -K_m x_m - R_m v_m + g f_i + P_{\mathrm{ED}} A_e, \tag{13a}$$

$$(M_s + M_r)\dot{v}_s = -(K_s + K_r)x_s - (R_s + R_r)v_s - f_i - P_{\mathrm{FL}} A_s, \tag{13b}$$

where $f_i = K_i(x_s - g x_m) + R_i(v_s - g v_m)$ is the force transferred through the ISJ. In the preceding equations, A_e and A_s are effective areas of the eardrum and the stapes footplate, respectively; x_m and v_m, respectively, denote the displacement and velocity of the malleal system, and x_s and v_s denote the displacement and the velocity of the stapes, respectively. Also, in Eq. (13b), parameters $\{M_r, R_r, K_r\}$ represent the round window.[6] The present middle-ear model is similar to that of Talmadge *et al.* (1998) except for a nonrigid ISJ here. Middle-ear frequency responses are reported in Appendix A.

III. SIMULATION METHODS

A. Fine-tuning cochlear parameters

Table I shows the parameters used in the present cochlear model: the values listed are for the base ($x=0$), the longitudinal midpoint ($x=L/2$), and the apex ($x=L$). Parameter values intermediate to these three locations were determined by log-quadratic interpolation.[7] These values were carefully chosen to produce (1) tonotopic mapping typical of humans, (2) cochlear excitation profiles and frequency responses typical of mammals, and (3) nonlinear compression of BM motion typical of mammals. Approximation formulas were derived from frequency-domain analysis to facilitate the parameter-tuning process; more details are described in Appendix B. Parameter values listed in Table I are a result of this fine-tuning process. Then, these parameters were used in simulation of DP and DP suppression.

B. Delivering the stimulus

To simulate experimental conditions in a typical DPOAE measurement paradigm, we assumed that the stimulus is delivered as a force $f(t)$ that acts on a diaphragm, the diaphragm is latched on one end to a coupler inserted in the ear canal; at the other end of the coupler is the eardrum. Therefore, the dynamics of the diaphragm are described by the following equation:

$$M_d \dot{v}_d = f(t) - R_d v_d - K_d x_d - P_d A_d, \tag{14}$$

where v_d and x_d denote the velocity and the displacement of the diaphragm, respectively, P_d denotes the pressure in the enclosed space, and A_d is the area of the diaphragm. Two further assumptions about the coupler were made: first, the coupler is acoustically lossless; second, the physical dimension of the coupler is much smaller than the shortest wavelengths of interest. Therefore, P_d is approximately equal to the pressure P_{ED} at the eardrum in Eq. (13a), and the enclosed volume of air is acoustically compliant:

$$P_d = K_c(x_d A_d - x_m A_e). \tag{15}$$

Parameter values were as follows:[8] $K_c = 8.5 \times 10^5$ dyn/cm^5, $M_d = 5 \times 10^{-3}$ g, $R_d = 1.4 \times 10^3$ g/s, $K_d = 4 \times 10^8$ g/s^2, and $A_d = 0.75$ cm^2.

C. State-space formulation and numerical integration in time

To conduct a time-domain simulation, a minimal set of variables (displacements, velocities, currents, or voltages) were selected as *state variables* so their rates of change could be determined instantaneously given their present state and the stimulus. Then, the state variables were integrated numerically with respect to time.

The following variables were chosen as state variables: diaphragm variables $\{x_d, v_d\}$, middle-ear variables $\{x_m, v_m, x_s, v_s\}$, and cochlear variables including RL displacement $\xi_r(x)$, RL velocity $u_r(x)$, OHC contraction velocity $u_o(x)$, OHC membrane potential $V(x)$, and the gating charge $Q(x)$. With some algebra, Eqs. (5)–(7) and (10) can be rearranged as follows:

$$\dot{\xi}_r(x) = u_r, \tag{16a}$$

$$\dot{Q}(x) = T^{-1}u_o, \tag{16b}$$

$$\dot{u}_r(x) = \frac{Ru_o + KTQ}{M} - \frac{V - C_g^{-1}Q}{TM} - \frac{r(u_r + u_o) + k(\xi_r + TQ)}{m} - \frac{P(x)}{m}, \tag{16c}$$

$$\dot{u}_o(x) = -\frac{Ru_o + KTQ}{M} + \frac{V - C_g^{-1}Q}{TM}, \tag{16d}$$

$$\dot{V}(x) = \frac{1}{C}(i_r(u_r, \xi_r) - GV - T^{-1}u_o). \tag{16e}$$

In Eq. (16e), $i_r(u_r, \xi_r)$ is the nonlinear function defined in Sec. II A. Note that although $P(x)$ on the right hand side of Eq. (16c) is not a state variable, it could be solved instantaneously given the state variables. By combining Eqs. (8) and (9), the following approximation was derived,

$$\partial_x^2 P = -\frac{\rho}{A}\left(\partial_x\partial_t U - \partial_t U\frac{\partial_x A}{A}\right), \tag{17a}$$

$$\approx -\frac{\rho}{A}w\partial_t^2\xi_r. \tag{17b}$$

The second term on the right hand side of Eq. (17a) was neglected, assuming that $A^{-1}\partial_x A \approx 0$ (i.e., the taper of the area is small compared to its overall size). Combining Eqs. (17b) and (16c), we obtained the following relation between $P(x)$ and state variables:

$$\left(\partial_x^2 - \frac{\rho w}{mA}\right)P = l\big(u_r(x), u_o(x), \xi_r(x), Q(x), V(x)\big), \tag{18}$$

where $l(\cdot)$ denotes a linear combination. Then, Eq. (18) with boundary conditions described in Sec. II C was solved numerically by a finite-difference method with $N=700$ discrete cochlear segments. The computation load was $O(N)$.[9]

To summarize, the *state vector* consisted of 3500 cochlear variables and six other variables, and their rates of change were determined by Eqs. (13), (14), (16), and (18) given their present state and the stimulus $f(t)$. Let us denote the state vector as $\mathbf{x}(t)$, and its time derivative as $\mathbf{v}(\mathbf{x})$. State-space equations were numerically integrated with respect to time in steps of $\Delta t = 6.25$ μs. For each step in time t, $\mathbf{x}(t)$ was updated by a modified Sielecki method (Diependaal *et al.*, 1987) in two steps; first, $\mathbf{x}(t+\Delta t)$ was estimated by extrapolation:

$$\hat{\mathbf{x}} = \mathbf{x} + \Delta t \cdot \mathbf{v}(\mathbf{x}). \tag{19}$$

Then, $\mathbf{v}$ was re-evaluated at $\hat{\mathbf{x}}$, and the state variables were updated as follows:

$$\mathbf{x}(t + \Delta t) = \mathbf{x}(t) + \Delta t \cdot \frac{\mathbf{v}(\mathbf{x}(t)) + \mathbf{v}(\hat{\mathbf{x}})}{2}. \tag{20}$$

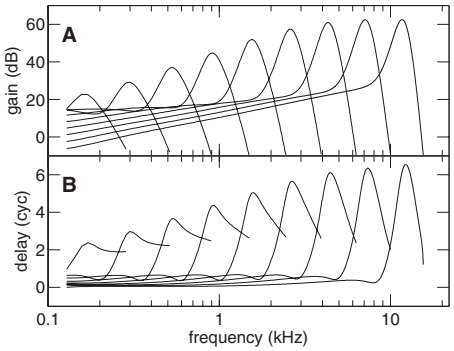

FIG. 2. Frequency responses at selected locations in the cochlea. Curves represent responses at nine different locations in equal distances: $x = \{0.9, 0.8, \ldots, 0.1\}$ times the length the cochlea, respectively. Characteristic frequency decreases as x increases (i.e., toward the apex). (A) RL-to-stapes displacement gain. (B) RL displacement group delay.

IV. RESPONSES TO STIMULI

A. Cochlear tuning and latency for low-level stimuli

To calculate cochlear tuning properties at low intensity, a wide-band (0.32–12 kHz) click was delivered to the diaphragm. The level of the click was set sufficiently low (peak-equivalent SPL $<$ 32 dB at the eardrum) so that the OHC receptor currents $i_r(t)$ were no more than 2.5% of $I_{\max}$ in Eq. (3) anytime and anywhere in the cochlea. The simulation ran for 70 ms, long enough for the traveling wave to reach the apical region of the cochlea.

In Fig. 2, the stapes-to-RL displacement gain and its group delay are plotted against frequency for nine different locations in the cochlea.[10] Characteristic frequency (CF) (i.e., frequency of maximum gain) decreases from base to apex. As shown in Fig. 2(A), the displacement gain at CF increases from 23 dB at the most apical location to 62 dB near the base. The group delay, when expressed in number of cycles, also reaches its maximum $N_{\max}$ near CF for every location.

By inspection, the responses in Fig. 2(A) are more sharply tuned at basal locations than apically. Further analyses show that the quality factor in terms of the *equivalent rectangular bandwidth*[11] (Q_{ERB}) increases from 1.8 to 9.9 from apex to base (Fig. 3, top panel). Between 0.5 and 10 kHz, the present values of Q_{ERB} are similar to those of cats and guinea pigs derived from auditory-nerve recordings (Shera *et al.*, 2002). The values are also similar to human Q_{ERB} values derived from DP suppression tuning data (Gorga *et al.*, 2008); however, they are smaller than the Q_{ERB} of humans derived from psychoacoustic experiments (Glasberg and Moore, 1990). Additionally, the model Q_{ERB} seems to flatten between 1 and 10 kHz, in agreement with older psychoacoustic findings but different from more recent data that suggest that (a) $Q_{\mathrm{ERB}} > 10$ for a wide range of frequencies, and (b) Q_{ERB} continues to increase at higher frequencies (Shera *et al.*, 2002).

The maximum group delay $N_{\max}$ for each location is plotted against CF in the bottom panel of Fig. 3, in comparison to cochlear latency estimated from stimulus-frequency otoacoustic emission (SFOAE) data across different species (Shera *et al.*, 2002). The model latency $N_{\max}$ is shorter than

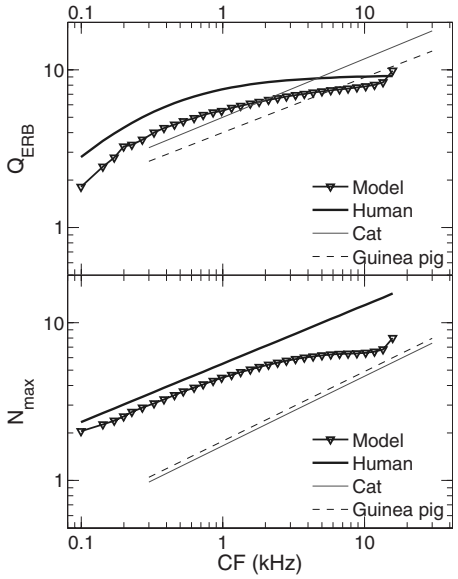

FIG. 3. Model Q_{ERB} (top panel) and latency N_{max} (bottom panel) plotted against characteristic frequency. Results are compared with curves derived from experimental data across three species. Human $Q_{ERB}=9.26CF/(CF+230\ Hz)$ is given by Glasberg and Moore (1990). Linear fits of human N_{max} and cat and guinea pig Q_{ERB} and N_{max} are given by Shera *et al.* (2002).

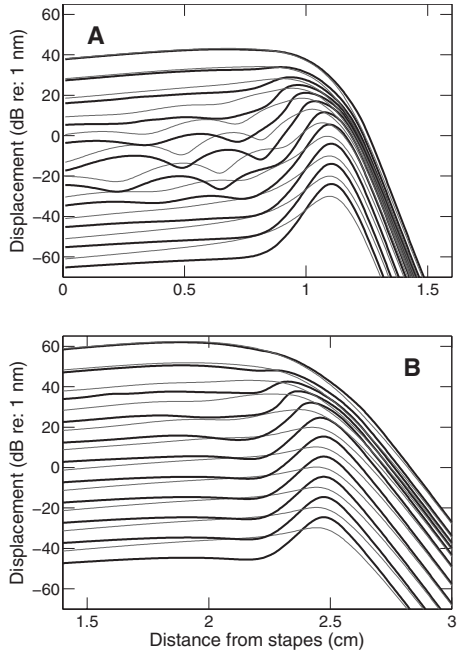

FIG. 4. Excitation patterns for pure-tone stimuli. BM displacement (thin lines) and RL displacement (thick lines) along the cochlea are plotted as the input level varies from 0 to 100 dB SPL in 10 dB steps. (A) Stimulus frequency $f_0=4$ kHz. (B) $f_0=500$ Hz.

that of human SFOAE forward latency but longer than that of cats and guinea pigs. Note that the model N_{max} also seem to flatten at above 1 kHz, a feature shared with the model Q_{ERB} but not observed in SFOAE data. The model latency, when expressed in absolute time, ranges from 7.0 ms at the 0.5 kHz place to 0.8 ms at the 8 kHz place. Compared to estimates of human cochlear forward latency based on auditory brainstem responses (Neely *et al.*, 1988; Harte *et al.*, 2009), the model latency is similar at 0.5 kHz but shorter at 8 kHz.

B. Compression of single tones

Figure 4 shows BM (thin lines) and RL (thick lines) magnitude responses to a single tone at two different frequencies for input levels L_0 from 0 to 100 dB sound pressure level (SPL) in 10 dB steps. The response plotted at every location is the magnitude of BM or RL displacement at the frequency of the stimulus f_0; harmonic distortions are omitted.

For each frequency, the magnitude response is compressed near its characteristic place (CP). For $f_0=4$ kHz, RL displacement at CP ($x=1.1$ cm) grows nearly linearly from $L_0=0$–30 dB (Fig. 5). When L_0 increases from 30 to 90 dB, the RL displacement at the CP increases only by an order of magnitude and the best place shifts toward the base (Rhode and Robles, 1974). For $f_0=500$ Hz, the response is nearly linear for $L_0\leq 40$ dB while the compression is more prominent for $L_0=50$–90 dB. The magnitude response is approximately linear near the base for $f_0=500$ Hz; the excitation pattern forms parallel lines for the first 2.0 cm from the stapes [Fig. 4(B)]. The near-linear growth at low intensity is consistent with recent experimental findings (Rhode, 2007, Fig. 1), in contrast to a cubic-root growth of amplitude predicted by "essential nonlinearity" (Eguíluz *et al.*, 2000) and Hopf bifurcation theory (Stoop and Kern, 2004). However, for $f_0=4$ kHz, this presumably linear growth is confounded by a standing-wave pattern that is prominent for $L_0=30$–70 dB. This standing-wave phenomenon indicates a reflection from the CP and was explained as a consequence of self-suppression of the forward-going waves for intermediate input levels (Kanis and de Boer, 1993, Fig. 2).

Compared to BM excitation patterns, the RL excitation patterns in Figs. 4(A) and 4(B) have higher tip-to-tail gains and are more sharply tuned. Since RL motion is more directly related to neural excitation, the present results suggest a distinction between tuning curves recorded from auditory nerves (e.g., Pfeiffer and Kim, 1975; van der Heijden and Joris, 2006) and BM tuning curves obtained by motion-sensing techniques (e.g., Rhode, 1971; Ruggero *et al.*, 1997).

Figure 5 shows the RL and BM displacements at CP as a function of stimulus level; their *rate of growth* (ROG), defined as the slope of the I/O function, is plotted in Fig. 6.

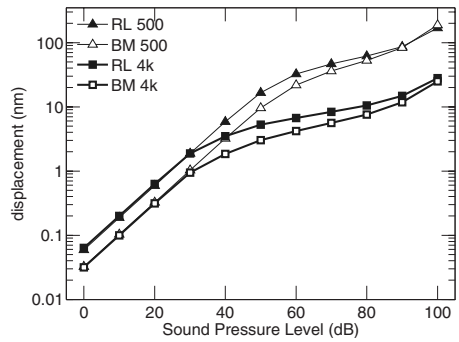

FIG. 5. Nonlinear growth of RL and BM displacements at CP, plotted against stimulus intensity. The stimulus is either a 4 kHz or a 500 Hz pure tone.

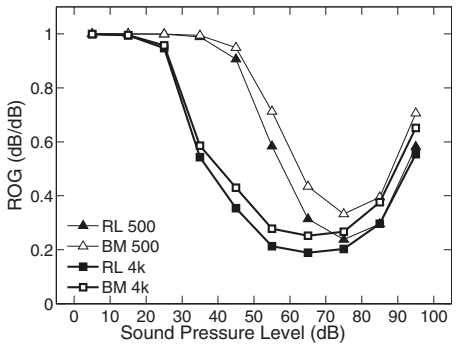

FIG. 6. RL and BM response rate of growth (ROG, see the text for definition), plotted against stimulus intensity.

As can be seen in Fig. 6, the response to 4 kHz stimuli is most compressive between 60 and 70 dB SPL, reaching a minimum ROG of 0.19 and 0.25 for RL and BM, respectively. The response to 500 Hz stimuli is linear for a more extended input range; the response is most compressive between 70 and 80 dB SPL, reaching minimum ROGs of 0.24 and 0.33 for RL and BM, respectively.

The model results for the 4 kHz stimuli have comparable ROG to BM vibration data from the 9 kHz place (Ruggero *et al.*, 1997, Fig. 3: ROG=0.2–0.5) and the 6 kHz place (Rhode, 2007, Fig. 3: ROG~0.3) in chinchilla cochleae. However, experimental results showed individual variability, and a more compressive BM response has also been reported (Rhode, 2007, Fig. 4: ROG~0.1).

C. Distortion-product otoacoustic emissions

To simulate DPOAE, the stimulus $f(t)$ was comprised of two tones at frequencies $\{f_1,f_2\}$ and levels $\{L_1,L_2\}$. The amplitude of the two tones was calibrated so that the SPL varied from 40 to 80 dB for L_1 and from 20 to 70 dB for L_2 in 2 dB steps, respectively. The range of L_2 is similar to that of a typical experiment on human subjects (e.g., Johnson *et al.*, 2006; Long *et al.*, 2009). A 5 ms cosine-square ramp was used for the onset of the stimulus. For each combination of $\{L_1,L_2\}$, the simulation ran for a sufficiently long time (more than the duration of the ramp plus 40 cycles of f_1) so that the DPOAE at the eardrum reached a steady level. Then, the magnitude L_d of DPOAE at $f_d=2f_1-f_2$ was calculated using discrete Fourier transform (DFT). The window length of DFT was set so that it contained minimal integer cycles of f_1 and f_2, respectively—for example, if f_2 is 4 kHz and $f_2/f_1=1.2$, the window length is 6 cycles of f_2, or 1.5 ms.

Results for 16 different conditions of primary frequencies $\{f_1,f_2\}$ are reported in Fig. 7: four f_2's (1, 2, 4, or 8 kHz) by four primary-frequency ratios ($f_2/f_1=1.4$, 1.3, 1.2, or 1.1). Each column represents a fixed f_2 and each row represents a fixed f_2/f_1. In each panel, isolevel contours for L_d as a function of L_1 and L_2 are plotted in 4 dB steps. Note that the contours are well rounded for $f_2/f_1=1.40$ across all f_2, and become more oblique and narrower as f_2/f_1 decreases. Therefore, for any fixed f_2 and L_2, the "optimal" L_1 that yields the highest DPOAE level has a tendency to decrease

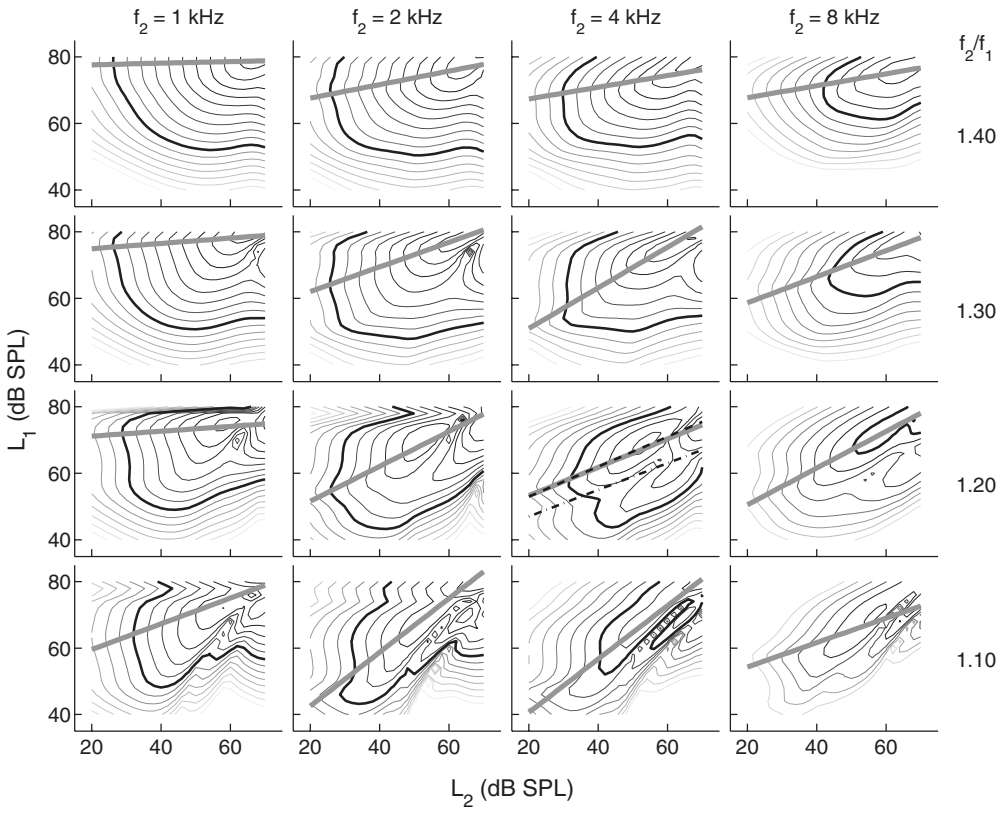

FIG. 7. DPOAE level L_d, plotted as a function of L_1 and L_2 for various combinations of $\{f_1,f_2\}$. Isolevel contours are plotted in 4 dB steps. As a reference, the contour corresponding to $L_d=0$ dB SPL is indicated with a thick black line. Otherwise, darker contours represent higher L_d. Only contours corresponding to $L_d>-30$ dB are shown. In each panel, the thick gray line represents linear regression of optimal L_1 as a function of L_2. Empirical optimal paths are shown on the panel for $f_2=4$ kHz and $f_2/f_1=1.20$ for comparison; dashed line was recommended by Neely *et al.* (2005), and dash-dotted line by Kummer *et al.* (1998).

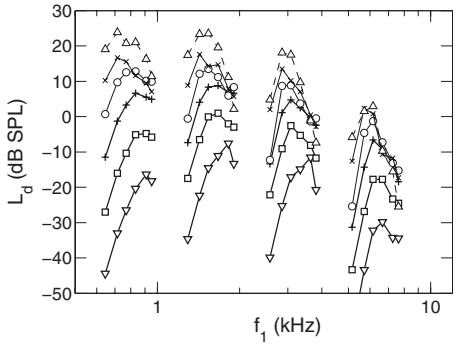

FIG. 8. DP filtering effects. DP level L_d is plotted against f_1 for a fixed f_2 =1, 2, 4, or 8 kHz. Curves marked with different symbols correspond to different L_2: ▽=20 (dB), □=30, +=40, ○=50, ×=60, and △=70, while $L_1=39+0.4L_2$.

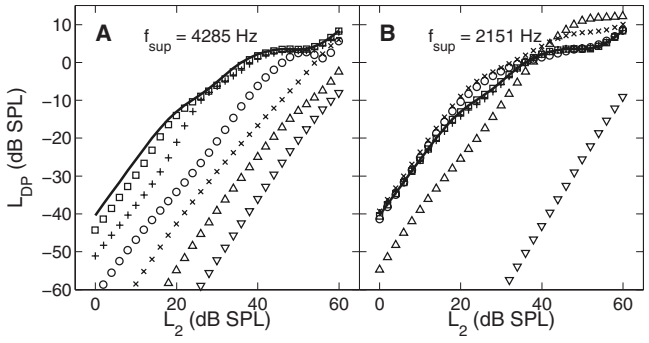

FIG. 9. Suppression of DPOAE by a third tone. Frequencies of the primary tones are: $f_2=4000$ Hz, and $f_1=f_2/1.22$. (A) "On-frequency" suppression, $f_{sup}\approx f_2$. (B) $f_{sup}\approx 0.5f_2$. In both panels, the solid line shows DP input-output (I/O) function with negligible suppression (suppressor level L_{sup} =0 dB). Symbols represent the I/O function for different L_{sup}: □=30, + =40, ○=50, ×=60, △=70, and ▽=80.

as f_2/f_1 decreases. This result agrees qualitatively with experimental data from normal-hearing humans (Johnson *et al.*, 2006). In each panel, the straight line shows a linear regression of optimal L_1 as a function of L_2. Among all linear paths shown in Fig. 7, the path for $f_2=4$ kHz and $f_2/f_1=1.20$ is $L_1=0.43L_2+45$, which comes closest to paths previously recommended. To obtain maximum DPOAE, Kummer *et al.* (1998) recommended the path of $L_1=0.4L_2+39$ and Neely *et al.* (2005) recommended $L_1=0.45L_2+44$.

Another way to visualize the DPOAE data is to plot L_d against primary frequencies. Following Kummer *et al.* (1998) recommendation, we set $L_1=0.4L_2+39$. DPOAE level L_d is plotted against f_1 for fixed $f_2=1$, 2, 4, or 8 kHz and fixed L_2 from 20 to 70 dB in 10 dB steps. In Fig. 8, each curve consists of six points corresponding to $f_2/f_1=1.55$, 1.4, 1.3, 1.2, 1.1, and 1.05, respectively. Results show that the optimal f_1 for each curve ranges from $f_2/1.4$ (e.g., for $f_2=1$ kHz, $L_2=60$ or 70 dB) to $f_2/1.1$ (e.g., for $f_2=2$ or 4 kHz, $L_2=20$ dB). Also, the optimal f_1 decreases as L_2 increases for $f_2=1$, 2, or 4 kHz.

Brown *et al.* (1992) reported human DPOAE at a fixed f_2 while f_1 was swept, so f_2/f_1 varied from 1.01 to 1.41. Primary levels were fixed at $L_2=40$ dB and $L_1=55$ dB. DP level was plotted against DP frequency f_d, and results showed a band-pass profile similar to Fig. 8 with a plateau of approximately 0.8 kHz wide and 5–10 dB (SPL) high. The peak level L_d for the $2f_1-f_2$ component occurred at an f_1 of approximately 3.3–3.4 kHz, which is higher than the best $f_1\approx 3.1$ kHz of the present model. This discrepancy will be discussed further in Sec. V.

D. Suppression of DPOAE

Model responses to three tones were tested in a DP suppression paradigm. The stimulus $f(t)$ consisted of two primary tones with $f_2/f_1=1.22$ and a suppressor tone at frequency f_{sup} and level L_{sup}. As L_2 varied, L_1 was set as recommended by Kummer *et al.* (1998): $L_1=0.4L_2+39$. The DP I/O function was measured in the same manner as described in Sec. IV C except that the window used for spectral analysis now contained minimal integer cycles of f_1, f_2, and f_{sup}.

Figure 9 shows DP I/O function for an "on-frequency" suppression condition [$f_{sup}\approx f_2$, Fig. 9(A)] and for f_{sup} at approximately one octave lower [Fig. 9(B)]. The thick line shows the DP I/O function when $L_{sup}=0$ dB SPL; at this suppressor level, any change of DP level due to the presence of the suppressor should be negligible. On-frequency suppression becomes prominent for $L_{sup}\geq 40$ dB SPL, and the I/O function generally shifts to the right as L_{sup} increases further. In contrast, the low-frequency suppressor does not cause L_d to reduce until $L_{sup}=70$ dB. Note that the low-frequency suppressor even causes L_d to increase for L_{sup} =50, 60, and 70 dB for different ranges of L_2. Possible reasons for this DPOAE increment induced by a low-frequency "suppressor" will be discussed in Sec. V.

The rightward shift of DP I/O function shown in Fig. 9 could be quantified by finding the input increment ΔL_2 necessary for the DP level L_d to reach a given level when the suppressor is present. In Fig. 10, ΔL_2 is plotted against L_{sup} for the on-frequency suppressor (filled symbols) and the low-frequency suppressor (open symbols) for L_d to reach −20 or −3 dB SPL. Results indicate that I/O curves begins to shift to the right ($\Delta L_2>0$) at a lower L_{sup} for $L_d=-20$ dB than for $L_d=-3$ dB; this is true for both the on-frequency and the

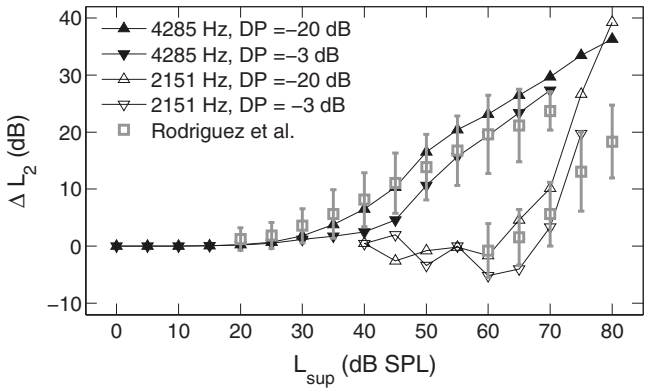

FIG. 10. DP input suppression. The increase ΔL_2 in input level required for DPOAE to reach a given level (−20 or −3 dB SPL) is plotted against suppressor level L_{sup}. Filled symbols represent the "on-frequency" suppression ($f_{sup}\approx f_2$). Open symbols represent f_{sup} at about one octave lower. Squares and error bars show means and standard deviations, respectively, of DP suppression data from normal-hearing humans (Rodríguez *et al.*, 2010).

low-frequency suppressors. The shift ΔL_2 produced by the present model is comparable to data from normal-hearing humans (Rodríguez *et al.*, 2010) for most of the lower L_{sup}'s. For the highest L_{sup} tested (70 dB for $f_{sup} \approx f_2$ and 75 or 80 dB for $f_{sup} \approx 0.5 f_2$), ΔL_2 produced by the model is at least one standard deviation higher than the mean in Rodríguez *et al.*'s data (in which ΔL_2 was measured with $L_d = -3$ dB SPL). This discrepancy will be discussed in Sec. V.

V. DISCUSSION

A. Cochlear tuning and parameter selection

Employing a frequency-domain analysis, we previously predicted that the present OHC model could provide amplification to the traveling waves in a frequency-selective manner (Liu and Neely, 2009) if parameters α_v (velocity sensitivity) and C_g (gating capacitance) are sufficiently large. During the parameter-selection process for the present study, we found that the tip-to-tail gain and the quality factor Q_{ERB} were both reduced when smaller values of α_v or C_g were used. In this sense, the present study serves as a time-domain confirmation of the frequency-domain analysis. Note that α_v and C_g represent different components of the "cochlear amplifier:" α_v represents the sensitivity of MET, which depends on the potential gradient across the apical membrane of the OHC; C_g depends on the density of motor molecules (*prestin*) on the OHC lateral membrane and is reduced when the cell is hyperpolarized (Santos-Sacchi, 1991). The present model makes it possible to investigate the relations between cochlear tuning properties and micromechanical parameters such as α_v and C_g. Simulation can be conducted to predict responses from cochleae with different types of OHC pathology. This might be of clinical interest and provides directions for future research.

In spite of the effort devoted to the parameter-selection process in order to make a tonotopic map typical of humans, the sharpness of tuning Q_{ERB} and the cochlear latency N_{max} produced by the present model (Fig. 3) fall below experimental values previously derived from human ears. Several other lines of evidence also suggest that the tuning of the present model is not as sharp as in human cochleae: first, the ratio f_2/f_1 that produces the highest DPOAE is higher in the present model than that obtained from normal-hearing human ears (Sec. IV C). This implies that the present model is not as sharply tuned as human cochleae because the cutoff frequency of the DP filter (Fig. 8) is an estimate of the bandwidth of cochlear responses. Second, in the present model, the low-frequency suppressor produces much more DPOAE suppression than empirically at high L_{sup} (Fig. 10). This indicates that the f_2 characteristic place in the present model has a larger response to low-frequency stimuli at high level than it does in human cochleae. Therefore, either the present model is less sharply tuned than human cochleae or its excitation pattern shifts toward the base excessively at high intensities. Further investigation is needed to explore these two possibilities.

The reduced sharpness of tuning may be a limitation of one-dimensional (long-wave) cochlear modeling. In a two-dimensional (2D) model, the real and imaginary parts of the wave propagation function, which are related to cochlear gain and cochlear latency respectively, are both greater than those predicted by a 1D model (Shera *et al.*, 2005). Kolston (2000) argued that it is necessary to model cochlear mechanics in three dimensions so as to match both the phase and the gain responses to experiment data. To increase the sharpness of tuning for the present 1D model, we could have set α_v or C_g to higher values. However, values higher than currently used might start to deviate from physical reality. Additionally, we found that higher α_v's resulted in spontaneous vibration in the cochlear partition, which could propagate from the cochlea as SOAE. The frequency of SOAE is hard to predict (Ku *et al.*, 2009), and its presence complicates spectral analysis since the present method assumed that the frequencies of all spectral components are of integer ratios. In the future, higher α_v values might be preferred to produce higher cochlear gain; an improved spectral-analysis method is also warranted.

B. Cochlear nonlinearities

In the present study, the gating capacitance of OHCs was linearized to confine the source of nonlinearity to MET of OHCs (see Sec. II B). Patuzzi (1996) argued that such simplification is legitimate at high frequencies because the response in OHC lateral-membrane potential is limited by membrane capacitance. However, at low frequencies and high intensities, Patuzzi (1996) stated that the membrane potential may change by tens of millivolts; in this case, the operating point shifts significantly, so the nonlinearity in OHC gating capacitance needs to be considered.

In light of Patuzzi's (1996) argument, we examined the maximum potential change elicited by acoustical stimuli in the present model. Results showed that the change in OHC membrane potential was indeed larger for low-frequency than for high-frequency stimuli, but was no more than 4.0 mV for single tones at 100 dB SPL at any frequency between 0.125 and 8 kHz. This amplitude was too small to have caused a significant shift in the OHC operating point. Though the model's findings deviated from Patuzzi's (1996) prediction, our attempt to linearize the dynamics of piezoelectrical membrane is justified as far as numerical simulation is concerned. Improving the representation of electrical properties of the OHC is an area for future work.

The present model reproduced, at least qualitatively, many features in nonlinear responses that are typical of humans and other mammals. We have argued that some discrepancies could be accounted for by increasing the sharpness of tuning throughout the cochlear model. Another discrepancy is in the absolute level of DPOAE; in Fig. 7, the DP level L_d reached >30 dB SPL for the highest L_1 and L_2 tested for $f_2 = 1$ or 2 kHz when $f_2/f_1 \geq 1.30$. In contrast, the mean of L_d across normal-hearing ears was never greater than 20 dB SPL as reported by Johnson *et al.* (2006). Nevertheless, the DP I/O function in Fig. 9(A) is similar to experimental data at $L_2 = 20-50$ dB SPL (Johnson *et al.*, 2006; Long *et al.*, 2009; Rodríguez *et al.*, 2010). While discrepancy of the absolute levels of DPOAE could be partially explained by transmission through the middle ear (see discussion in

Appendix A), discrepancy in the DP growth rate at high L_2 indicates that the nonlinearity in the present model is not sufficiently compressive.

Note that the DP level discrepancy becomes prominent at $L_2 \geq 50$ dB, at which the medial olivocochlear (MOC) efferent inhibition would be activated (Guinan, 2006). A recent study also showed that middle-ear muscle reflex (MEMR) was elicited by a 75 dB activator at 1 kHz in 25% of normal-hearing ears (Keefe *et al.*, 2010). It is possible that MOC efferents and MEMR both contribute to the suppression of DPOAE level when L_1 or L_2 is above their respective thresholds. Therefore, incorporating these negative feedback mechanisms to the present model may help reduce the excessive DPOAE it generates at high primary levels.

As stated previously, the one-dimensional treatment is known to affect tuning. Because tuning is related to compression in a nonlinear model, the absence of close quantitative agreement with experimental data could also be related to the simplified dimensionality of the present model.

C. Negative suppression

The *negative suppression* shown in Figs. 9(B) and 10 remains puzzling. It occurred only for a certain input range (50–70 dB). In fact, negative suppression of DPOAE has been observed empirically; for instance, the mean input suppression ΔL_2 in Rodríguez *et al.* (2010) is -0.8 dB at $L_{sup} = 60$ dB for the low-frequency suppressor. To explain Rodríguez *et al.*'s (2010) data, one can assume that the DP wavelets from the f_2 characteristic place and those reflected coherently (Zweig and Shera, 1995) from the DP place interfere destructively at the stapes. When a low-frequency suppressor is presented at an intermediate level, it reduces the wavelets that originate from the DP place and releases DPOAE from wave cancellation. This causes the DPOAE level to increase.

An alternative explanation for negative suppression is that the suppressor causes DP to be reflected from its characteristic place in a nonlinear fashion, much similar to the reflection observed in Fig. 4 and by Kanis and de Boer (1993). If the reflected wavelets interfere with the wavelets from the f_2 place *constructively*, there would be an increase in the level of DPOAE. In theory, waves are scattered wherever there is an impedance mismatch. If saturation nonlinearity causes the propagation-gain function to reduce locally at a high intensity, the wavenumber function should also be altered due to causality (Shera, 2007). Similarly, it may be possible to investigate how characteristic impedance is altered locally and waves scattered nonlinearly, perhaps using a quasilinear approach (Kanis and de Boer, 1993; Talmadge *et al.*, 1998). In the future, a time-domain model such as presented in this paper can serve as a numerical test bench for theories developed in this direction.

VI. CONCLUSIONS

Simulation of DPOAE at frequency $2f_1 - f_2$ can be achieved by introducing an antisymmetric nonlinearity to the MET channel of OHCs. The present nonlinear OHC models embedded in a one-dimensional transmission-line cochlear model collectively produce dynamic-range compression, broadening of excitation patterns, and shifting of excitation patterns toward the base, similar to responses observed in live mammalian cochleae. The model also produces DPOAE isolevel contour plots that vary with f_1 and f_2, DP band-pass filtering effects across three octaves of f_2, and a shift of DPOAE I/O functions due to suppression by a third tone. Several lines of evidence suggest that the present model is, however, less sharply tuned than human cochleae. The present results might be improved by setting a higher sensitivity of OHC receptor current with respect to RL velocity or by modeling mechanics of the cochlear fluid in two or three dimensions. Nevertheless, qualitative similarities between the present results and experimental data from normal-hearing ears suggest that the model may also be useful for studying other nonlinear responses in healthy cochleae. In addition, because of an explicit representation of OHC electromechanics, it is possible to alter parameters for the present model and simulate responses in ears with different types of OHC pathology. These provide directions for future research.

ACKNOWLEDGMENTS

We gratefully acknowledge two anonymous reviewers for providing valuable comments. We also thank Joyce Rodríguez and Emery Ku for giving critiques on previous versions of this manuscript. This study was supported by a grant from NIH-NIDCD (Grant No. R01-DC8318).

APPENDIX A: MIDDLE-EAR TRANSFER FUNCTIONS

Figure 11 shows middle-ear transfer functions in both the forward and the reverse direction. Results were obtained from a finite-difference, frequency-domain version of the present cochlear model. First, cochlear input impedance Z_c was calculated using a small-signal analysis (Puria and Allen, 1991), i.e., Eq. (1) was used instead of Eq. (2). Given Z_c, we drew an equivalent circuit for the middle-ear mechanics (Fig. 1) and derived the forward pressure transfer function S_{12}, defined as the acoustic pressure gain from the ear canal to the cochlear vestibule (Puria, 2003). To calculate transfer functions in the reverse direction, we assumed that the ear canal has an acoustic impedance of $\rho c/A$—ρ is the air density, c is the speed of sound, and A is the cross-sectional area of the ear canal; in other words, reflection of reverse-traveling sounds was ignored. The equivalent circuit was also used for calculation of the reverse pressure transfer function S_{21}, defined as the ratio of the ear canal pressure to the cochlear fluid pressure for reverse transmission. Finally, the reverse middle-ear impedance M_3, defined as the ratio of the vestibule pressure to the stapes volume velocity, was calculated. For comparison purposes, the symbols and definitions are borrowed from a previous study (Puria, 2003, Fig. 2).

The main discrepancy between the present results and human cadaver data is in the phase responses of pressure transfer functions. The phase accumulated to more than 300° for both S_{12} and S_{21} in Puria's (2003) data, and in one case more than 540° for S_{12} in Nakajima *et al.* (2009). This indicates a middle-ear latency, in the order of tens of μs (Dong

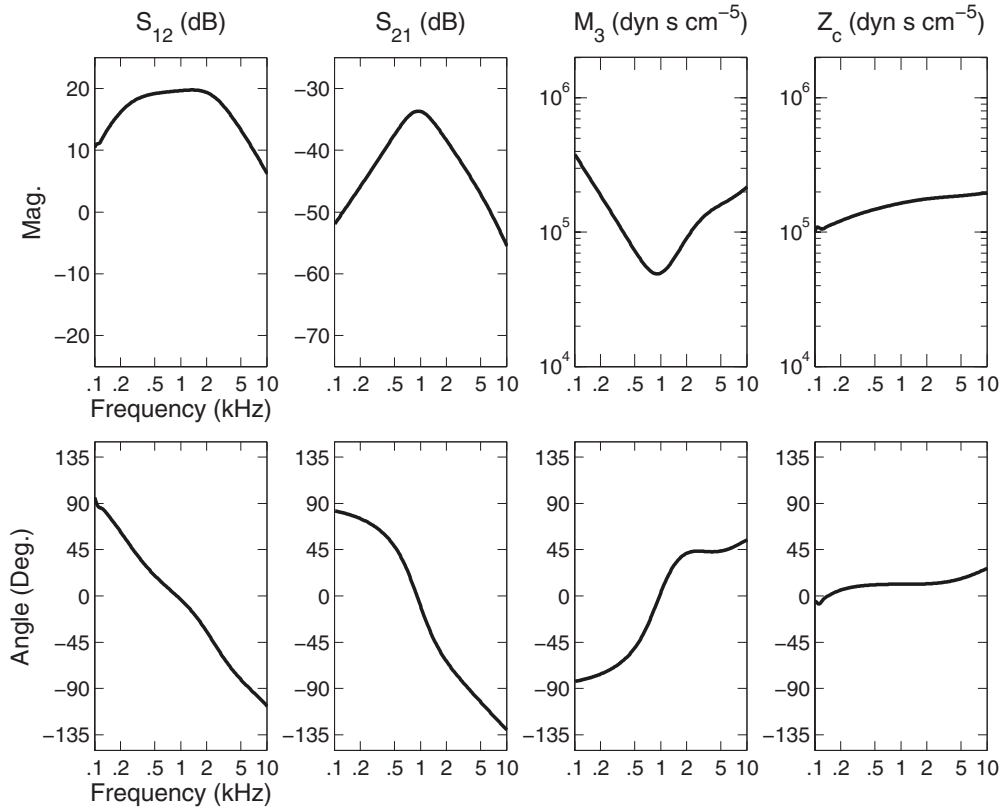

FIG. 11. Middle-ear transfer functions. Top panels show magnitude responses, and bottom panels show phase responses. From left to right, the four columns show forward pressure transfer function (S_{12}), reverse pressure transfer function (S_{21}), reverse middle-ear impedance (M_3), and the cochlear input impedance Z_c, respectively.

and Olson, 2006), that is not present in our model but has been attributed to tympanic membrane dynamics (Puria and Allen, 1998).

Compared to measurements from human cadavers (Puria, 2003; Nakajima *et al.*, 2009), the magnitude plateau in S_{12} is about the same height (10–20 dB gain). The width of the plateau is similar to Nakajima *et al.* (2009) (their Fig. 6) but appears wider than in Puria's data (his Fig. 2); the present S_{12} is as much as 10–15 dB higher at frequencies below 500 Hz and above 4 kHz. The magnitude of S_{21} are similar to Puria's (2003) result, peaking at around 1 kHz and rolls off approximately to -50 and -60 dB at 0.1 and 10 kHz, respectively. However, the maximum $|S_{21}|$ is smaller than Puria's (2003) but more similar to results from live gerbils (Dong and Olson, 2006, Fig. 5).

The magnitude of S_{12} and S_{21} influences the level of DPOAE directly (Keefe and Abdala, 2007). If the middle-ear parameters are adjusted to reduce S_{12} and match Puria's (2003) data, it will require higher L_1 and L_2 to achieve the same levels of DP inside the cochlea. Consequently, we can expect the DP contours to shift toward the upper-right corner in Fig. 7, more so for f_2=4 or 8 kHz than for 1 and 2 kHz. However, S_{12} and S_{21} are interdependent due to reciprocity; reducing S_{12} tends to increase S_{21}. It remains to be studied how much the difference between model-predicted DPOAE levels and those measured from normal-hearing humans (Johnson *et al.*, 2006, Fig. 1) can be resolved by jointly adjusting S_{12} and S_{21}.

APPENDIX B: METHODS FOR ADJUSTING THE COCHLEAR PARAMETERS

For a stimulus at sufficiently low intensity, the response at any given location in the cochlea can be characterized by three salient frequencies: a *shoulder frequency* f_{sh} above which the magnitude increases rapidly, a *pole frequency* f_p at which the response reaches its peak, and a *cutoff frequency* f_c at which the response starts to roll off. Based on the present assumptions on fluid coupling [Eq. (9)] and OHC electromechanics, these frequencies are approximately given by the following formulas:

$$2\pi f_{sh} = \sqrt{K_{eq}/M}, \tag{B1a}$$

$$2\pi f_p = \sqrt{(K_{eq} + \alpha_v/TC)/M}, \tag{B1b}$$

$$2\pi f_c = \sqrt{k/m}, \tag{B1c}$$

where $K_{eq}=K+(T^2C)^{-1}+(T^2C_g)^{-1}$. For negative damping to occur, it is necessary that $f_{sh}<f_p<f_c$ (Liu and Neely, 2009). Further, large capacitances C and C_g and high sensitivity α_v are preferred to achieve high amplification (Liu and Neely, 2009). All parameters listed in Table I were fine-tuned while maintaining that $f_p<f_c$ but maximizing α_v/TC so as to ensure a broad negative damping region. In Fig. 12, salient frequencies are compared against Greenwood's function (Greenwood, 1990) and the CF predicted by the present model. The model-predicted CF follows the pole frequency closely. Also, the CF does not deviate from Greenwood's

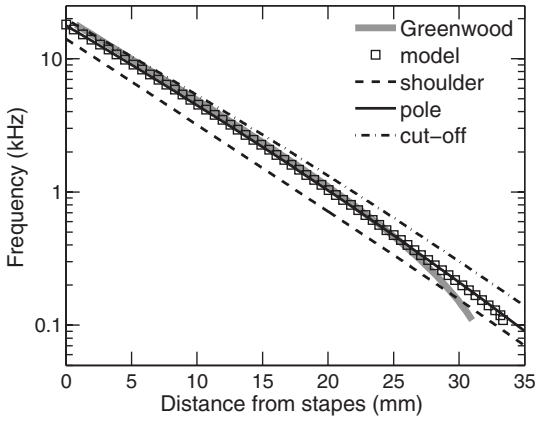

FIG. 12. Place-frequency functions. The shoulder frequency, the pole frequency, and the cutoff frequency were calculated as a function of distance from stapes. At selected places, the model-predicted CF is marked with a square. The Greenwood function was defined as $\mathrm{CF}(x)=F_0\cdot 2^{-x/l}-F_1$, where x is the distance from stapes, $l=5.0$ mm, $F_0=20$ kHz, and $F_1=0.165$ kHz.

function (Greenwood, 1990) by more than 10% except at the most apical 7 mm. The discrepancy there reflects the limitation of fitting the parameters spatially by log-quadratic interpolation (Sec. III A).

Finally, the parameter $I_{\max}$ which characterizes nonlinearity [see Eq. (3)] was adjusted to produce reasonable dynamic-range compression and DP I/O function. We found that a small $I_{\max}$ produces compression at low stimulus levels but limits the maximum DP level. Thus, $I_{\max}$ and middle-ear transfer functions S_{12} and S_{21} jointly affect the amount of DPOAEs produced by the present model.

[1]That is, any phase advance of i_r relative to ξ_r due to radial coupling between OHC hair bundles and the tectorial membrane was represented by the velocity-sensing parameter α_v [see Sec. VC of Liu and Neely (2009) for more discussion].

[2]Because Eq. (3) is antisymmetric, all the even-order terms vanish in its Taylor expansion around the origin. Consequently, even-order DPs vanish while odd-order products remain.

[3]In our previous study (Liu and Neely, 2009), an OHC was assumed to stretch against RL on one side, BM on the other side, and the stiffness of the OHC itself. We then argued that, because the stiffness of BM is much higher than that of RL, the impedance is approximately that of RL for the frequency range of interest. Therefore, the effective mass M and resistance R in Eq. (7) can be regarded as equivalent to the RL mass and resistance, whereas the effective stiffness K is equivalent to OHC stiffness plus RL stiffness in Liu and Neely (2009).

[4]Alternatively, Liu and Neely (2009) assumed that the volume velocity gradient couples to the velocity of both the RL and the BM; i.e., $\partial_x U=w(\dot{\xi}_r+\dot{\xi}_b)$. Empirically, Eq. (9) gives higher displacement gain in the cochlea.

[5]Hereafter, *acoustic pressure* is referred to as *pressure* for simplicity.

[6]Equation (13b) implicitly assumes that the displacement of the round window is equal to that of the stapes but in the opposite direction, and that the area of the round window is the same as the area of the stapes.

[7]Let q_0, q_1, and q_2 denote the value of a parameter q at the base, the midpoint, and the apex respectively. Then, $q(x)$ was calculated using the following formula: $q(x)=q_0\exp[ax(L-x)+bx]$, where $a=2\log(q_1^2/q_0q_2)/L^2$ and $b=\log(q_2/q_0)/L$.

[8]K_c corresponds to the acoustic compliance of enclosed air of 1.7 cm^3 at atmospheric pressure. Diaphragm parameters K_d, R_d, and M_d were chosen arbitrarily to produce a sufficiently flat response in the frequency range of interest. Note that the resonance frequency of the diaphragm, $\sqrt{K_d/M_d}/2\pi$, is above 40 kHz, and the Q-value ($\sqrt{K_dM_d}/R_d$) is about 1.0.

[9]Thus, the spatial resolution δ along the x-direction was 50 μm, and $\partial_x^2 P$ was approximated by $[P(x+\delta)-2P(x)+P(x-\delta)]/\delta^2$. So, Eq. (18) was solved by inverting a tridiagonal matrix via Gaussian elimination, which has a computation load of $O(N)$.

[10]To derive the gain and the group delay, the Fourier transform $X_r(x,f)$ of RL displacement $\xi_r(x,t)$ was calculated at every location x. Define a transfer function $T(x,f)=X_r(x,f)/X_s(f)$, where $X_s(f)$ is the Fourier transform of stapes displacement $x_s(t)$. The displacement gain plotted in Fig. 2(A) is $|T(x,f)|$ in dB, and the group delay plotted in Fig. 2(B) is defined as $N=-f\partial_f\phi$, where ϕ denotes the phase of $T(x,f)$.

[11]For an arbitrary tuning curve $T(f)$, its ERB is defined as $\Delta f=\int_0^\infty|T(f)|df/T_{\max}$, where $T_{\max}$ denotes the maximum of $|T(f)|$. Accordingly, Q_{ERB} is defined as $f_{\max}/\Delta f$, where $f_{\max}$ denotes the best frequency.

Brown, A. M., Gaskill, S. A., and Williams, D. M. (**1992**). "Mechanical filtering of sound in the inner ear," Proc. R. Soc. London, Ser. B **250**, 29–34.

Brownell, W. E., Bader, C. R., Bertrand, D., and de Ribaupierre, Y. (**1985**). "Evoked mechanical responses of isolated cochlear hair cells," Science **227**, 194–196.

Corey, D. P., and Hudspeth, A. J. (**1983**). "Kinetics of the receptor current in bullfrog saccular hair cells," J. Neurosci. **3**, 962–976.

Dallos, P. (**1973**). *The Auditory Periphery: Biophysics and Physiology* (Academic, New York).

Dallos, P. (**2008**). "Cochlear amplification, outer hair cells and prestin," Curr. Opin. Neurobiol. **18**, 370–376.

Davis, H. (**1983**). "An active process in cochlear mechanics," Hear. Res. **9**, 79–90.

Diependaal, R. J., Duifhuis, H., Hoogstraten, H. W., and Viergever, M. A. (**1987**). "Numerical methods for solving one-dimensional cochlear models in the time domain," J. Acoust. Soc. Am. **82**, 1655–1666.

Dong, W., and Olson, E. S. (**2006**). "Middle ear forward and reverse transmission in gerbil," J. Neurophysiol. **95**, 2951–2961.

Dong, W., and Olson, E. S. (**2008**). "Supporting evidence for reverse cochlear traveling waves," J. Acoust. Soc. Am. **123**, 222–240.

Eguíluz, V. M., Ospeck, M., Choe, Y., Hudspeth, A. J., and Magnasco, M. O. (**2000**). "Essential nonlinearities in hearing," Phys. Rev. Lett. **84**, 5232–5235.

Gaskill, S. A., and Brown, A. M. (**1990**). "The behaviour of the acoustic distortion product, 2f1-f2, from the human ear and its relation to auditory sensitivity," J. Acoust. Soc. Am. **88**, 821–839.

Glasberg, B. R., and Moore, B. C. J. (**1990**). "Derivation of auditory filter shapes from notched-noise data," Hear. Res. **47**, 103–138.

Gorga, M. P., Neely, S. T., Dierking, D. M., Kopun, J., Jolkowski, K., Groenenboom, K., Tan, H., and Stiegemann, B. (**2008**). "Low-frequency and high-frequency distortion product otoacoustic emission suppression in humans," J. Acoust. Soc. Am. **123**, 2172–2190.

Greenwood, D. D. (**1990**). "A cochlear frequency-position function for several species—29 years later," J. Acoust. Soc. Am. **87**, 2592–2605.

Guinan, J. J., Jr. (**2006**). "Olivocochlear efferents: Anatomy, physiology, function, and the measurement of efferent effects in humans," Ear Hear. **27**, 589–607.

Hall, J. L. (**1974**). "Two-tone distortion products in a nonlinear model of the basilar membrane," J. Acoust. Soc. Am. **56**, 1818–1828.

Harte, J. M., Pigasse, G., and Dau, T. (**2009**). "Comparison of cochlear delay estimates using otoacoustic emissions and auditory brainstem responses," J. Acoust. Soc. Am. **126**, 1291–1301.

Hubbard, A. E., Mountain, D. C., and Chen, F. (**2003**). "Time-domain responses from a nonlinear sandwich model of the cochlea," in *Biophysics of the Cochlea: From Molecules to Models*, edited by A. W. Gummer (World Scientific, Singapore), pp. 351–358.

Hudspeth, A. J. (**1997**). "Mechanical amplification of stimuli by hair cells," Curr. Opin. Neurobiol. **7**, 480–486.

Johnson, T. A., Neely, S. T., Garner, C. A., and Gorga, M. P. (**2006**). "Influence of primary-level and primary-frequency ratios on human distortion product otoacoustic emissions," J. Acoust. Soc. Am. **119**, 418–428.

Kanis, L. J., and de Boer, E. (**1993**). "Self-suppression in a locally active nonlinear model of the cochlea: A quasi-linear approach," J. Acoust. Soc. Am. **94**, 3199–3206.

Keefe, D. H., and Abdala, C. (**2007**). "Theory of forward and reverse middle-ear transmission applied to otoacoustic emissions in infant and adult ears," J. Acoust. Soc. Am. **121**, 978–993.

Keefe, D. H., Fitzpatrick, D., Liu, Y.-W., Sanford, C. A., and Gorga, M. P. (**2010**). "Wideband acoustic reflex test in a test battery to predict middle-ear dysfunction," Hear. Res. In press.

Kemp, D. T. (**1978**). "Stimulated acoustic emissions from within the human

auditory system," J. Acoust. Soc. Am. **64**, 1386–1391.
Kim, D. O., Molnar, C. E., and Mathews, J. W. (**1980**). "Cochlear mechanics: Nonlinear behavior in two-tone responses as reflected in cochlear-nerve-fibre responses and in ear canal sound pressure," J. Acoust. Soc. Am. **67**, 1704–1721.
Kim, D. O., Molnar, C. E., and Pfeiffer, R. R. (**1973**). "A system of nonlinear differential equations modeling basilar-membrane motion," J. Acoust. Soc. Am. **54**, 1517–1529.
Kolston, P. J. (**2000**). "The importance of phase data and model dimensionality to cochlear mechanics," Hear. Res. **145**, 25–36.
Ku, E. M., Elliott, S. J., and Lineton, B. (**2009**). "Limit cycle oscillations in a nonlinear state space model of the human cochlea," J. Acoust. Soc. Am. **126**, 739–750.
Kummer, P., Janssen, T., and Arnold, W. (**1998**). "The level and growth behavior of the 2f1-f2 distortion product otoacoustic emission and its relationship to auditory sensitivity in normal hearing and cochlear hearing loss," J. Acoust. Soc. Am. **103**, 3431–3444.
Liu, Y.-W., and Neely, S. T. (**2009**). "Outer hair cell electromechanical properties in a nonlinear piezoelectric model," J. Acoust. Soc. Am. **126**, 751–761.
Long, G. R., Jeung, C., and Talmadge, C. L. (**2009**). "Dependence of distortion-product otoacoustic emission components on primary-level ratio," in *Concepts and Challenges in the Biophysics of Hearing*, edited by N. P. Cooper and D. T. Kemp (World Scientific, Singapore), pp. 203–208.
Lu, T. K., Zhak, S., Dallos, P., and Sarpeshkar, R. (**2006**). "Fast cochlear amplification with slow outer hair cells," Hear. Res. **214**, 45–67.
Matthews, J. W. (**1983**). "Modeling reverse middle ear transmission of acoustic distortion signals," in *Mechanics of Hearing*, edited by E. de Boer and M. A. Viergever (Delft University Press, Delft), pp. 11–18.
Nakajima, H. H., Dong, W., Olson, E. S., Merchant, S. N., Ravicz, M., and Rosowski, J. J. (**2009**). "Differential intracochlear sound pressure measurements in normal human temporal bones," J. Assoc. Res. Otolaryngol. **10**, 23–36.
Neely, S. T. (**1988**). "Transient responses in an active, nonlinear model of cochlear mechanics," in *Basic Issues in Hearing*, edited by D. Duifuis, J. Horst, and H. Wit (Academic, New York).
Neely, S. T. (**1993**). "A model of cochlear mechanics with outer hair cell motility," J. Acoust. Soc. Am. **94**, 137–146.
Neely, S. T., Gorga, M. P., and Dorn, P. A. (**2000**). "Distortion product and loudness growth in an active, nonlinear model of cochlear mechanics," in *Recent Developments in Auditory Mechanics*, edited by H. Wada, T. Takasaka, K. Ikeda, K. Ohyama, and T. Koike (World-Scientific, Singapore), pp. 237–243.
Neely, S. T., Johnson, T. A., and Gorga, M. P. (**2005**). "Distortion-product otoacoustic emission measured with continuously varying stimulus level," J. Acoust. Soc. Am. **117**, 1248–1259.
Neely, S. T., and Kim, D. O. (**1983**). "An active cochlear model showing sharp tuning and high sensitivity," Hear. Res. **9**, 123–130.
Neely, S. T., and Kim, D. O. (**1986**). "A model for active elements in cochlear biomechanics," J. Acoust. Soc. Am. **79**, 1472–1480.
Neely, S. T., and Liu, Y.-W. (**2009**). "Retrograde propagation of cochlear distortion," in *Concepts and Challenges in the Biophysics of Hearing*, edited by N. P. Cooper and D. T. Kemp (World Scientific, Singapore), pp. 55–61.
Neely, S. T., Norton, S. J., Gorga, M. P., and Jesteadt, W. (**1988**). "Latency of auditory brain-stem responses and otoacoustic emissions using tone-burst stimuli," J. Acoust. Soc. Am. **83**, 652–656.
Neely, S. T., and Stover, L. J. (**1994**). "Otoacoustic emissions from a nonlinear, active model of cochlear mechanics," in *Biophysics of Hair Cell Sensory Systems*, edited by H. Duifhuis, J. W. Horst, P. van Dijk, and S. M. van Netten (World Scientific, Singapore), pp. 64–71.
Nobili, R., Vetešník, A., Turicchia, L., and Mammano, F. (**2003**). "Otoacoustic emissions from residual oscillations of the cochlear basilar membrane in a human ear model," J. Assoc. Res. Otolaryngol. **4**, 478–494.
Patuzzi, R. (**1996**). "Cochlear micromechanics and macromechanics," in *The Cochlea*, edited by P. Dallos, A. N. Popper, and R. R. Fay (Springer, New York), pp. 186–257.
Pfeiffer, R. R., and Kim, D. O. (**1975**). "Cochlear nerve fiber responses: Distribution along the cochlear partition," J. Acoust. Soc. Am. **58**, 867–869.
Puria, S. (**2003**). "Measurements of human middle ear forward and reverse acoustics: Implications for otoacoustic emissions," J. Acoust. Soc. Am. **113**, 2773–2789.
Puria, S., and Allen, J. B. (**1991**). "A parametric study of cochlear input impedance," J. Acoust. Soc. Am. **89**, 287–309.
Puria, S., and Allen, J. B. (**1998**). "Measurement and model of the cat middle ear: Evidence of tympanic membrane acoustic delay," J. Acoust. Soc. Am. **104**, 3463–3482.
Rabbitt, R. D., Clifford, S., Breneman, K. D., Farrell, B., and Brownell, W. E. (**2009**). "Power efficiency of outer hair cell somatic electromotility," PLOS Comput. Biol. **5**, e1000444.
Ramamoorthy, S., Deo, N. V., and Grosh, K. (**2007**). "A mechano-electro-acoustical model for the cochlea: Response to acoustic stimuli," J. Acoust. Soc. Am. **121**, 2758–2773.
Ren, T. (**2004**). "Reverse propagation of sound in the gerbil cochlea," Nat. Neurosci. **7**, 333–334.
Rhode, W. S. (**1971**). "Observations of the vibration of the basilar membrane in squirrel monkeys using the Mössbauer technique," J. Acoust. Soc. Am. **49**, 1218–1231.
Rhode, W. S. (**2007**). "Basilar membrane mechanics in the 6–9 kHz region of sensitive chinchilla cochleae," J. Acoust. Soc. Am. **121**, 2792–2804.
Rhode, W. S., and Robles, L. (**1974**). "Evidence from Mössbauer experiments for nonlinear vibration in the cochlea," J. Acoust. Soc. Am. **55**, 588–596.
Ricci, A. J., Kennedy, H. J., Crawford, A. C., and Fettiplace, R. (**2005**). "The transduction channel filter in auditory hair cells," J. Neurosci. **25**, 7831–7839.
Rodríguez, J., Neely, S. T., Patra, H., Kopun, J., Jesteadt, W., Tan, H., and Gorga, M. P. (**2010**). "The role of suppression in psychophysical tone-on-tone masking," J. Acoust. Soc. Am. **127**, 361–369.
Ruggero, M. A., Rich, N. C., and Robles, L. (**1997**). "Basilar-membrane responses to tones at the base of the chinchilla cochlea," J. Acoust. Soc. Am. **101**, 2151–2163.
Santos-Sacchi, J. (**1991**). "Reversible inhibition of voltage-dependent outer hair cell motility and capacitance," J. Neurosci. **11**, 3096–3110.
Shera, C. A. (**2007**). "Laser amplification with a twist: Traveling-wave propagation and gain functions from throughout the cochlea," J. Acoust. Soc. Am. **122**, 2738–2758.
Shera, C. A., Guinan, J. J., Jr., and Oxenham, A. J. (**2002**). "Revised estimates of human cochlear tuning from otoacoustic and behavioral measurements," Proc. Natl. Acad. Sci. U.S.A. **99**, 3318–3323.
Shera, C. A., Tubis, A., and Talmadge, C. L. (**2005**). "Coherent reflection in a two-dimensional cochlea: Short-wave versus long-wave scattering in the generation of reflection-source otoacoustic emissions," J. Acoust. Soc. Am. **118**, 287–313.
Shera, C. A., Tubis, A., Talmadge, C. L., de Boer, E., Fahey, P. F., and Guinan, J. J., Jr. (**2007**). "Allen-Fahey and related experiments support the predominance of cochlear slow-wave otoacoustic emissions," J. Acoust. Soc. Am. **121**, 1564–1575.
Stoop, R., and Kern, A. (**2004**). "Two-tone suppression and combination tone generation as computations performed by the Hopf cochlea," Phys. Rev. Lett. **93**, 268103.
Talmadge, C. L., Tubis, A., Long, G. R., and Piskorski, P. (**1998**). "Modeling otoacoustic emission and hearing threshold fine structures," J. Acoust. Soc. Am. **104**, 1517–1543.
van der Heijden, M., and Joris, P. X. (**2006**). "Panoramic measurements of the apex of the cochlea," J. Neurosci. **26**, 11462–11473.
Zhang, Y., Kim, C. K., Lee, K. J. B., and Park, Y. (**2009**). "A Brownian energy depot model of the basilar membrane oscillation with a braking mechanism," Eur. Phys. J. E **29**, 345–349.
Zurek, P. M., Clark, W. W., and Kim, D. O. (**1982**). "The behavior of acoustic distortion products in the ear canals of chinchillas with normal or damaged ears," J. Acoust. Soc. Am. **72**, 774–780.
Zweig, G., and Shera, C. A. (**1995**). "The origin of periodicity in the spectrum of evoked otoacoustic emissions," J. Acoust. Soc. Am. **98**, 2018–2047.
Zwislocki, J. (**1962**). "Analysis of the middle-ear function. Part I: Input impedance," J. Acoust. Soc. Am. **34**, 1514–1523.